ChemComm

ROYAL SOCIETY OF CHEMISTRY

COMMUNICATION

View Article Online
View Journal | View Issue

Check for updates

Cite this: *Chem. Commun.*, 2025, **61**, 2568

Received 30th December 2024,
Accepted 9th January 2025

DOI: 10.1039/d4cc06791f

rsc.li/chemcomm

Revealing the CO_2 adsorption blocking mechanism in flexible low-silica small-pore zeolites *via* three-dimensional electron diffraction†

Jian Guo,[ab] Chenyang Nie,[bc] Shitai Li,[bc] Nana Yan,*[b] Peng Guo *[bc] and Zhongmin Liu[abc]

Low-silica small-pore zeolites are essential for CO_2 selective adsorption; however, some Na-form flexible types exhibit negligible performance. Advanced three-dimensional electron diffraction elucidated the blocking mechanism: Na^+ ions in elliptical 8-rings hinder CO_2 diffusion. Structural insights guided the design of K-form types with wider 8-rings, achieving enhanced CO_2 adsorption.

Carbon dioxide (CO_2) is a greenhouse gas, and its massive emissions lead to significant climate and environmental issues. Major sources of CO_2 emissions include coal-fired power generation, coal-bed methane and natural gas extraction, vehicle emissions, and landfills.[1] CO_2 is often mixed with other gases; for example, flue gas from coal-fired power plants contains over 70% N_2, about 10–15% CO_2, and trace amounts of other gases.[2] In recent years, the porous materials studied for CO_2/CH_4 and CO_2/N_2 separation mainly include metal–organic frameworks (MOFs), carbon-based materials, zeolites, covalent organic frameworks (COFs), porous organic solids, and others.[2–7] Among them, conventional zeolites are still attracting increasing attention due to their easy preparation, low cost, and good hydrothermal stability.[8] They are composed of SiO_4 and AlO_4 tetrahedra sharing vertex oxygen atom, forming regular channel or cage structures. In particular, the low Si/Al ratio small-pore zeolites with 8-ring pore openings, whose negative charges are balanced by inorganic cations, often exhibit high selectivity in the separation of CO_2/N_2 and CO_2/CH_4.

Up to now, small pore zeolites with various topologies have been utilized to investigate CO_2 adsorption.[9–14] For instance, in a rigid **CHA**-type zeolite with a Si/Al ratio of 2.2, the 8-ring apertures fully occupied by Cs^+ ions promote selective CO_2 adsorption.[9] The strong affinity between CO_2 and Cs^+ ions, due to the significant quadrupole moment of CO_2, triggers Cs^+ transitions that open a "trapdoor" for CO_2. In contrast, CH_4, with weaker interactions and larger kinetic diameters, cannot open this "trapdoor," resulting in high CO_2 selectivity over CH_4. For the flexible low-silica small-pore zeolites such as **RHO**-,[11] **MER**-,[12,15] **GIS**-,[13,16,17] and **PHI**-type,[14] the CO_2 adsorption mechanism becomes much more complex. From the structural point of view, these topologies consist of 4-ring chain fragments, and their CO_2 adsorption behaviour is often attributed to the combined effects of structural "breathing" and the trapdoor mechanism. For example, **RHO**-type zeolite is the classic one in the flexible zeolite family and it is composed of double 8-rings and *lta* cages as composite building units (CBUs). The flexibility of the **RHO**-type zeolites is characterized by the distortion of the double 8-ring from circular to elliptical upon dehydration.[11] It is worth noting that the type of inorganic cations and Si/Al ratio play crucial roles in the CO_2 adsorption.[11,15,16] For instance, Na-form **RHO**-type zeolite with a Si/Al ratio of 3.9 (denoted as Na-RHO) could adsorb CO_2 up to 3.07 mmol g^{-1} at 0.1 bar, which is much higher than that of K-RHO and Cs-RHO (both lower than 2 mmol g^{-1}).[11] Furthermore, the Si/Al ratio exerts a considerable influence on the CO_2 adsorption performance of flexible zeolites. For the K-MER zeolite at 1 bar, CO_2 adsorption gradually increases to 3.8 mmol g^{-1} as the Si/Al ratio rises ($1.7 < \text{Si/Al ratio} < 3.8$).[15] Thus, many endeavours have been devoted to investigating the diverse structural flexibility of zeolites with higher Si/Al ratio. In contrast, flexible small-pore zeolites with lower Si/Al ratios often exhibit negligible CO_2 uptake at 1 bar.[16,18] The underlying blocking mechanism for this phenomenon remains elusive and is closely associated with their crystallographic structures.

Traditionally, structural analysis of crystalline porous materials relies on single crystal X-ray diffraction (SC-XRD) and powder X-ray diffraction (PXRD). However, SC-XRD is limited

---

[a] *Henan Institute of Advanced Technology, Zhengzhou University, Zhengzhou 450001, China*
[b] *National Engineering Research Center of Lower-Carbon Catalysis Technology, Dalian Institute of Chemical Physics, Chinese Academy of Sciences, Dalian 116023, Liaoning, China. E-mail: yannana@dicp.ac.cn, pguo@dicp.ac.cn*
[c] *University of Chinese Academy of Sciences, Beijing 100049, China*

† Electronic supplementary information (ESI) available. CCDC 2385938–2385940 and 2402481. For ESI and crystallographic data in CIF or other electronic format see DOI: **https://doi.org/10.1039/d4cc06791f**

by the need for sample size, requiring crystals in the micrometre range, while PXRD provides one-dimensional (1D) diffraction patterns that often suffer from overlapping peaks, hindering precise intensity extraction. In recent years, a promising technique known as three-dimensional electron diffraction (3D ED) has been developed to determine the crystallo graphic structures of nanocrystals.[19–22] Compared to X-rays, the electron beams have a shorter wavelength and interact more strongly with the sample, making 3D ED suitable for solving the structure of nanosized crystals. The recently emerging continuous rotation electron diffraction (cRED), a 3D ED technique, enables the continuous and rapid collection of ED data from a single isolated nanocrystal.[23] It has demonstrated its power in solving crystallographic structures of various nano-sized zeolites with fascinating topologies.[24–28] However, its application in structural analysis of flexible zeolites is still rare.

In this article, we reveal the blocking mechanism of Na^+ exchanged low Si/Al ratio **GIS**- and **PHI**-type zeolites using the cRED technique. Dehydration of Na-form zeolites with significantly elliptical 8-rings hinders the diffusion of CO_2. Inspired by structural insights revealed by 3D ED, K-form **GIS**- and **PHI**-type zeolites were designed and further structural analysis revealed that the wider 8-ring pore openings resulting from the longer K–O bond distances significantly enhanced the CO_2 adsorption performance.

To investigate the CO_2 adsorption behaviour and uncover the blocking mechanism, Na-form **GIS**-type zeolite with a Si/Al ratio of 1.8 (denoted as Na-GIS) (Table S1, ESI†) was synthesized through a conventional hydrothermal method. The synthesis was performed at 100 °C under rotation at 50 rpm for 3 days, with a chemical gel composition of $4.68Na_2O:1.0Al_2O_3:8SiO_2:184H_2O$. The PXRD pattern and SEM images indicate that the as-synthesized Na-GIS zeolites are well-crystallized, exhibiting irregular polyhedral morphologies with dimensions of approximately 4 μm (Fig. S1, ESI†). It is worth noting that the CO_2 isothermal adsorption at 298 K (Fig. 1a) reveals that it hardly adsorbs CO_2 (0.04 mmol g^{-1}), which is consistent with the previous reports.[17]

To understand the blocking mechanism at the atomic level, 3D ED data was collected from an isolated nanocrystal using the cRED technique. It is important to note that data collection was performed within the intrinsic high vacuum (10^{-5} Pa) of transmission electron microscopy (TEM). This environment facilitates the dehydration of Na-GIS (denoted as Na-GIS-DH). This process effectively simulated the sample's state after activation for subsequent CO_2 adsorption experiments. The high-quality 3D ED dataset of Na-GIS-DH was collected by the cRED technique and the 3D reciprocal lattice was reconstructed as demonstrated in Fig. 1b. The tetragonal unit cell parameters of Na-GIS-DH were obtained and the possible space groups ($P4_32_12$ or $P4_12_12$) could be deduced based on the reflection conditions in Fig. 1c–e. Its initial structural model was solved by SHELXT with the space group assigned as $P4_12_12$. The idealized **GIS**-type framework is considered as the assembly by *gis* composite building units (CBUs) through sharing 8-rings (3.2 Å × 4.4 Å), as shown in Fig. 2a–c. The final structural refinement of Na-GIS-DH revealed significant distortions in the framework (Fig. 2d and Table S2, ESI†). Compared with the circular 8-ring pore openings in the idealized **GIS**-type framework, the pore openings in Na-GIS-DH become highly elliptical (1.8 Å × 6.2 Å), with Na^+ clearly identified at these sites (Fig. 2e and f). This indicates that these elliptical 8-rings in the Na-GIS-DH unraveled by cRED are too narrow for CO_2 molecules to pass through, resulting in negligible CO_2 uptake.

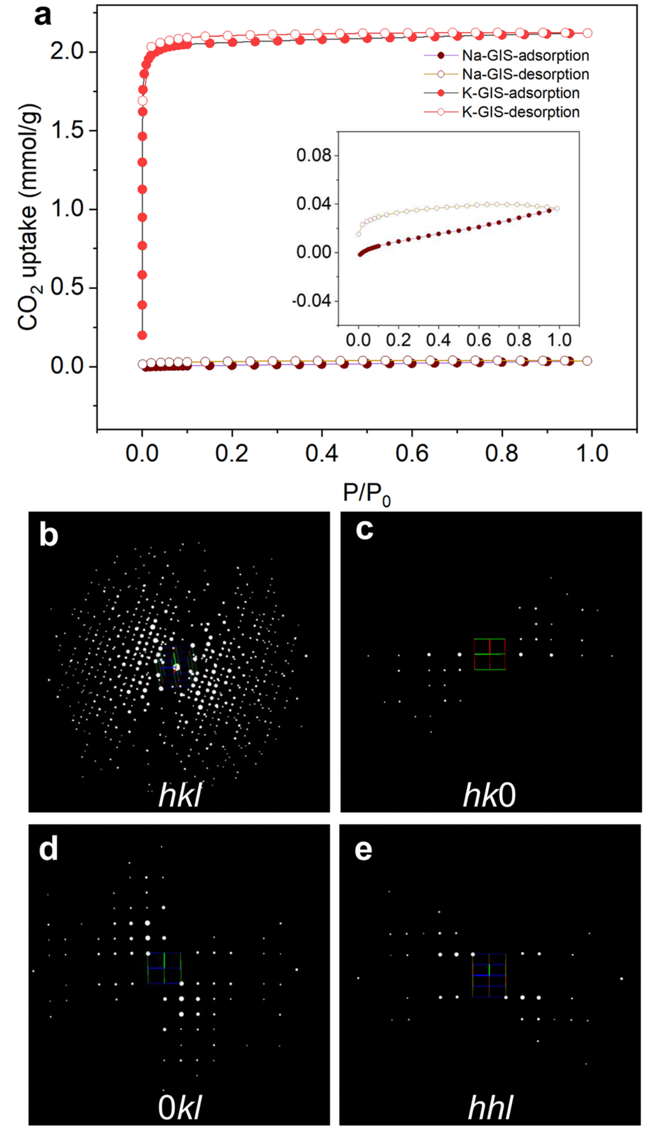

Fig. 1 (a) CO_2 adsorption isotherms of Na-GIS-DH (brown) and K-GIS-DH (red) at 298 K. (b) 3D reconstructed reciprocal lattice of Na-GIS-DH. (c)–(e) Three slices *hk*0, 0*kl*, and *hhl* extracted from the reconstructed reciprocal lattice.

In order to test our idea, we prepared K^+ ion-exchanged **GIS**-type zeolites (denoted as K-GIS). Because the K^+ has a larger ion radius than Na^+, it should have wider pore openings if the K^+ ions locate near the 8-ring pore openings. The 3D ED data of dehydrated K-GIS (denoted as K-GIS-DH) were collected under the same conditions as those for Na-GIS-DH. The initial structural model of K-GIS-DH was solved based on such high-quality

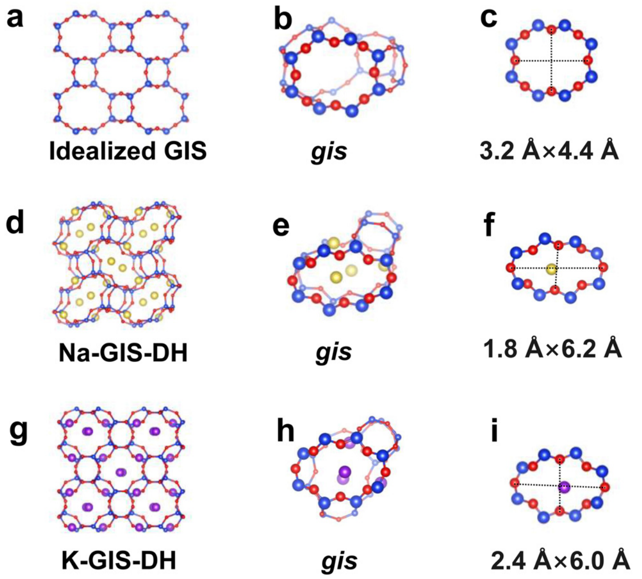

Fig. 2 Crystallographic structure (a), *gis* CBU (b), and 8-ring pore openings (c) in the idealized GIS-type framework. (d)–(f) Na-GIS-DH. (g)–(i) K-GIS-DH. The Si/Al, O, Na, and K are shown in blue, red, yellow, and purple, respectively. The aperture sizes of the 8-ring pore openings were determined by measuring the minimum and maximum distances between oxygen atoms, as indicated by the black dotted lines, and then subtracting the ionic diameter of O^{2-} (2.7 Å).

3D ED data and final refinement results are listed in Fig. S2 and Table S3 (ESI†). The results demonstrate that the framework of K-GIS-DH is also distorted (Fig. 2g). Notably, the two facing 8-rings of the *gis* CBUs become elliptical, adopting a crossed configuration (Fig. 2h). The K^+ ions are located near the centre of the 8-rings (2.4 Å × 6.0 Å) as displayed in Fig. 2i, which are wider than those of Na-GIS-DH. This widening occurs because the K–O bond distance is longer than the Na–O bond distance. Therefore, its CO_2 adsorption capacity was up to 2.12 mmol g^{-1} at 298 K and 1 bar (Fig. 1a), which is greatly enhanced compared with Na-GIS-DH. Besides, the adsorption sites of CO_2 molecules were also analysed using simulated annealing (Fig. S3, ESI†).[29] The results indicate that CO_2 molecules preferentially locate in the *gis* cage or K^+-free 8-ring openings. In order to test the dynamic separation performance of K-GIS, breakthrough experiments of binary CO_2/N_2 (15/85, v/v) and CO_2/CH_4 (5/95, v/v) were carried out at 25 °C and 1 bar, respectively. The corresponding breakthrough curves are shown in Fig. S4 (ESI†). Both N_2 and CH_4 broke through the separation column immediately. For CO_2/N_2 breakthrough, the dynamic adsorption capacity reaches 1.8 mmol g^{-1} for CO_2 and 0.2 mmol g^{-1} for N_2, with a retention time of 37 min g^{-1}, and a dynamic separation factor of 50.7. In the case of CO_2/CH_4 breakthrough, CH_4 adsorption is negligible, while the CO_2 capacity remains 1.8 mmol g^{-1} with an extended retention time of 142 min g^{-1}, which makes K-GIS have an almost infinite selectivity for CO_2/CH_4 (Table S4, ESI†). The above results indicate that K-GIS has the potential for selective CO_2 adsorption in practical applications.

We believe that this CO_2 adsorption blocking phenomenon is a general characteristic of flexible low-silica small-pore zeolites and does not only occur in **GIS**-type zeolites. Therefore, we prepared another Na-form low-silica small pore **PHI**-type zeolite. This zeolite was synthesized through inter-zeolite transformation under crystallization at 100 °C for 3 days (details in the ESI†). The Si/Al ratio of the final products is approximately 1.75, exhibiting prismatic morphology of 2–5 μm (Fig. S5, ESI†). Na-form **PHI**-type zeolites after dehydration (denoted as Na-PHI-DH) also show negligible CO_2 uptake (0.07 mmol g^{-1}) at 298 K and 1 bar (Fig. 3a). This low CO_2 uptake is similar to that observed for Na-GIS-DH. From a structural perspective, the idealized **PHI**-type framework consists of *phi* and *oto* cages, which are formed 3D channels through 8-rings with sizes of 4.3 Å × 4.4 Å, 3.0 Å × 3.5 Å, and 3.2 Å × 4.1 Å, respectively (Fig. S6, ESI†). The crystallographic structure of Na-PHI-DH determined by the cRED technique displays that 8-ring pore openings are distorted to an ellipse and reduced in size relative to the idealized **PHI**-type framework and Na^+ ions are located near the centre of the 8-ring pore (Fig. 3b, c and Fig. S7, Tables S5, S6, ESI†). There are four types of deformed 8-ring pore openings, as shown in Fig. 3c. Except for type II 8-ring openings, the short axis of other 8-ring pore openings is not larger than 1.8 Å.

Interestingly, the K^+ ion-exchange **PHI**-type zeolite after dehydration (designated as K-PHI) demonstrates that the corresponding 8-rings are larger than those observed in the

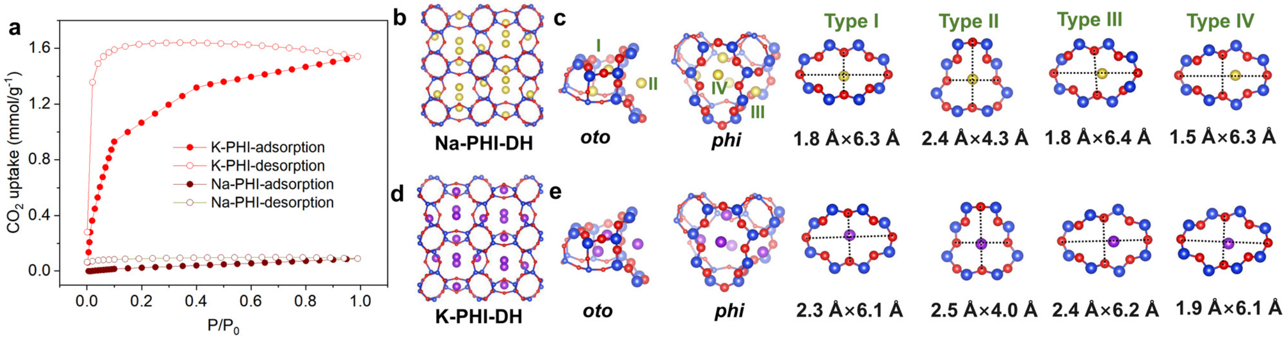

Fig. 3 (a) CO_2 adsorption isotherms of Na-PHI (brown) and K-PHI (red) at 298 K. The structures of (b) and (c) Na-PHI-DH and (d) and (e) K-PHI-DH framework, *oto* and *phi* CBUs, 8-ring pore openings (from left to right). The Si/Al, O, Na, and K are shown in blue, red, yellow, and purple, respectively.

Na-PHI-DH (Fig. 3d, e and Fig. S8, Table S7, ESI†). Meanwhile, its smallest pore size is 1.9 Å × 6.1 Å, which is still wider than all 8-rings in Na-PHI-DH, except type II. These wider pore openings enable CO_2 to pass through, resulting in an enhanced CO_2 adsorption capacity of 1.54 mmol g^{-1} (Fig. 3a) compared with Na-PHI-DH.

In this work, the CO_2 adsorption blocking mechanism of Na-form **GIS**- and **PHI**-type zeolites with a lower Si/Al ratio is elucidated by using the advanced 3D ED technique. This mechanism is attributed to their structural flexibility after dehydration, which leads to highly elliptical 8-ring pore openings that prevent CO_2 molecules from passing through at 1 bar. By understanding such blocking mechanisms, it enables us to design K-form **GIS**- and **PHI**-type zeolites for CO_2 adsorption. Importantly, the locations of Na^+ ions, K^+ ions, and CO_2 were determined through 3D ED combined with simulated annealing. K^+ ions in both zeolites are located near the 8-ring pores, and their longer K–O bond length results in wider 8-ring openings, enabling CO_2 diffusion through the pores. Uncovering the blocking mechanism is essential for understanding the adsorption mechanisms and facilitating the design of high-performance adsorbents.

This work is supported by the National Natural Science Foundation of China (No. 22288101, 22102177 and 22372156).

Data availability

The data supporting this article have been included as part of the ESI.†

Conflicts of interest

There are no conflicts to declare.

Notes and references

1 M. Yusuf and H. Ibrahim, *J. Environ. Chem. Eng.*, 2023, **11**, 111393.
2 Y. S. Bae and R. Q. Snurr, *Angew. Chem., Int. Ed.*, 2011, **50**, 11586–11596.
3 L. Paz, S. Gentil, V. Fierro and A. Celzard, *J. Environ. Chem. Eng.*, 2024, **12**, 114870.
4 E. Perez-Botella, S. Valencia and F. Rey, *Chem. Rev.*, 2022, **122**, 17647–17695.
5 X. Wang, N. Yan, M. Xie, P. Liu, P. Bai, H. Su, B. Wang, Y. Wang, L. Li, T. Cheng, P. Guo, W. Yan and J. Yu, *Chem. Sci.*, 2021, **12**, 8803–8810.
6 B. Chen, H. Xie, L. Shen, Y. Xu, M. Zhang, M. Zhou, B. Li, R. Li and H. Lin, *Small*, 2023, **19**, e2207313.
7 J. Wu, F. Xu, S. Li, P. Ma, X. Zhang, Q. Liu, R. Fu and D. Wu, *Adv. Mater.*, 2019, **31**, e1802922.
8 H. S. Lee, N. S. Kim, D. I. Kwon, S. K. Lee, M. Numan, T. Jung, K. Cho, M. Mazur, H. S. Cho and C. Jo, *Adv. Mater.*, 2021, **33**, e2105398.
9 J. Shang, G. Li, R. Singh, Q. Gu, K. M. Nairn, T. J. Bastow, N. Medhekar, C. M. Doherty, A. J. Hill, J. Z. Liu and P. A. Webley, *J. Am. Chem. Soc.*, 2012, **134**, 19246–19253.
10 Q. Liu, A. Mace, Z. Bacsik, J. Sun, A. Laaksonen and N. Hedin, *Chem. Commun.*, 2010, **46**, 4502–4504.
11 M. M. Lozinska, E. Mangano, J. P. Mowat, A. M. Shepherd, R. F. Howe, S. P. Thompson, J. E. Parker, S. Brandani and P. A. Wright, *J. Am. Chem. Soc.*, 2012, **134**, 17628–17642.
12 V. M. Georgieva, E. L. Bruce, M. C. Verbraeken, A. R. Scott, W. J. Casteel, Jr., S. Brandani and P. A. Wright, *J. Am. Chem. Soc.*, 2019, **141**, 12744–12759.
13 H. J. Choi, J. G. Min, S. H. Ahn, J. Shin, S. B. Hong, S. Radhakrishnan, C. V. Chandran, R. G. Bell, E. Breynaert and C. E. A. Kirschhock, *Mater. Horiz.*, 2020, **7**, 1528–1532.
14 H. J. Choi, E. L. Bruce, K. S. Kencana, J. Hong, P. A. Wright and S. B. Hong, *Angew. Chem., Int. Ed.*, 2023, **62**, e202305816.
15 H. J. Choi, D. Jo, J. G. Min and S. B. Hong, *Angew. Chem., Int. Ed.*, 2021, **60**, 4307–4314.
16 H. J. Choi and S. B. Hong, *Chem. Eng. J.*, 2022, **433**, 133800.
17 G. Deng, K. Cheng, B. Meng, X. Shi, X. Liu, Y. Zhou and J. Wang, *Sep. Purif. Technol.*, 2024, **340**, 126764.
18 Y. Liang, A. J. Jacobson and J. D. Rimer, *Microporous Mesoporous Mater.*, 2023, **353**, 112511.
19 U. Kolb, T. Gorelik, C. Kubel, M. T. Otten and D. Hubert, *Ultramicroscopy*, 2007, **107**, 507–513.
20 D. Zhang, P. Oleynikov, S. Hovmöller and X. Zou, *Z. Kristallogr. - Cryst. Mater.*, 2010, **225**, 94–102.
21 W. Wan, J. Sun, J. Su, S. Hovmoller and X. Zou, *J. Appl. Crystallogr.*, 2013, **46**, 1863–1873.
22 P. Guo, J. Shin, A. G. Greenaway, J. G. Min, J. Su, H. J. Choi, L. Liu, P. A. Cox, S. B. Hong, P. A. Wright and X. Zou, *Nature*, 2015, **524**, 74–78.
23 Y. Wang, S. Takki, O. Cheung, H. Xu, W. Wan, L. Öhrström and A. K. Inge, *Chem. Commun.*, 2017, **53**, 7018–7021.
24 C. Nie, N. Yan, C. Liao, C. Ma, X. Liu, J. Wang, G. Li, P. Guo and Z. Liu, *J. Am. Chem. Soc.*, 2024, **146**, 10257–10262.
25 Q.-F. Lin, Z. R. Gao, C. Lin, S. Zhang, J. Chen, Z. Li, X. Liu, W. Fan, J. Li, X. Chen, M. A. Camblor and F.-J. Chen, *Science*, 2021, **374**, 1605–1608.
26 J. I. Tirado, A. Sala, A. Bordes, P. Pratim Das, L. Palatinus, S. Nicolopoulos, J. L. Jorda, A. Vidal-Moya, T. Blasco, G. Sastre, S. Valencia and F. Rey, *Angew. Chem., Int. Ed.*, 2024, e202416515.
27 X. Liu, L. Liu, T. Pan, N. Yan, X. Dong, Y. Li, L. Chen, P. Tian, Y. Han, P. Guo and Z. Liu, *Angew. Chem., Int. Ed.*, 2021, **60**, 24227–24233.
28 C. Ma, P. Guo and Z. Liu, *Chin. J. Struct. Chem.*, 2024, **43**, 100235.
29 P. Krokidas, E. D. Skouras, V. Nikolakis and V. N. Burganos, *Mol. Simul.*, 2008, **34**, 1299–1309.